ACS OMEGA

Open Access



http://pubs.acs.org/journal/acsodf

Article

# Improving the Dust Removal Efficiency of a Natural Gas Filter: An Experimental and Numerical Simulation Study

Sijia Zheng,* Zhixiang Dai, Feng Wang, Qin Bie, Xinyi Wang, Xubing Liu, and Lin Zhong

Cite This: *ACS Omega* 2023, 8, 36986−36998

Read Online

ACCESS | Metrics & More | Article Recommendations

**ABSTRACT:** This study aims to evaluate the dust removal efficiency and working conditions of a filter separator through a pressure drop under various operating conditions. Typical horizontal filter separators in natural gas stations were taken as the research objects, and the computational fluid dynamics method was first attempted to investigate the static and dynamic characteristics of the pressure drop and the dust removal efficiency under different operating times and pressures. Then, the simulated results were compared with those obtained from online dust detection. At a constant standard flow rate, the detected pressure drop deviated from the fitted optimal quadratic curve with an increase in the operation duration of the filter separator, and the dust removal efficiency also tended to decline. The declining trend was particularly faster at lower operating pressures caused by the fast air flow, which leads to more coalesced particles flowing out and increases the dust concentration downstream. A higher initial pressure drop of the filter separator was also maintained at a low operating pressure. The dust removal efficiency rapidly decreased at a higher throughput load, and the decreasing rate became moderate at a lower input load. An optimum operating throughput of the filter was obtained when the input load varied in the range of $100 \times 10^4$−$270 \times 10^4$ $Nm^3/d$. Good agreement was achieved between the simulated and experimental dust removal efficiency, and the relative errors are within ±20%. Both methods applied in this work were verified to have high accuracy and reliability through the actual on-site amount of dust captured.

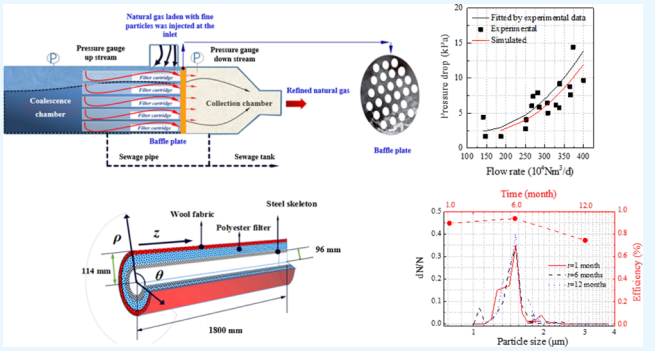


## 1. INTRODUCTION

A filter separator is often used to remove dust particles in the gas transmission.[1] Certain pressure drop inevitably occurs when dust particles are filtered, and the dynamic changes of the pressure drop can reflect the remaining lifetime of a filter separator.[2−4] It is necessary to evaluate the dust removal efficiency and working conditions based on the pressure drop performance.[5]

It is widely recognized that there are two stages in processing the particle filtration in the solid−gas system.[6] When the effect of the particle coalescence is not taken into account at the earlier stage, its effect on the separator structure and the collection efficiency can be neglected, and the penetration rate and the pressure drop will not change with the operational time. However, after a long time of operation, the penetration rate and the pressure drop will change with the operational time when the particles continuously coalesce on the surface of the cartridge and the chain structure finally forms and grows up quickly. Many scholars have dedicated efforts to discovering this phenomenon. Thomas et al.[7] have found that the particles always form a dendrite structure at the inner part of the filter where the pressure drop grows slowly with a fast increasing collection efficiency at the earlier stage. Then, a pressure surge will occur in the filter, which leads to a lower increasing speed of the collection efficiency. This phenomenon was further verified by Song et al.[8] by conducting experiments with monodisperse PSL particles. Ali et al.[9] assumed that a large number of filter separators in natural gas stations still suffer from the timing in replacing the elements, which is the main problem in optimization use of the filter. Since the pressure drop presents a dynamic equilibrium among capture, coalescence, and drainage, the pressure drop with the operational time is an important indicator to declare whether the filter cartridge should be replaced, especially when both the operational pressure and flow rate data were recorded and analyzed. Azam et al.[10] established the relationship between the pressure drop and separation efficiency of different filter materials. They found that the pressure drops increased with

Received: June 14, 2023
Accepted: September 5, 2023
Published: September 29, 2023

an increase in the bed thickness, and the pressure drop increased sharply when the porosity was less than 75%. Liu et al.[11] monitored the dust removal efficiency of a filter separator in a high-sulfur gas field by using a high-pressure natural gas particle online detection device. It is found that the dust removal efficiency and pressure drop suddenly increased exponentially when the application time reached 1/3 of the total service life. Lim et al.[12] reported that the pressure drop and particle removal efficiency increased by 30% when the porosity of a filter material was less than 50% of its original porosity. Song et al.[8] clarified the relationships among the dust removal efficiency of the filter element, pressure drop, and dust collection volume. They observed that the dust collection efficiency increased by 3 to 5 times when a "chain structure" formed on the filter element's fiber. However, the service life of the filter element was frequently affected by the chain structure. Riefler et al.[13] experimentally found the quadratic power relationship between the quality of the filter element and the dust removal efficiency. Thereafter, Thomas et al.[14,15] verified that this quadratic power relationship is universal. Bourrous et al.[16] clarified that the pressure drop of a filter separator is linearly related to the flow rate. The slope of this relationship, $k$, is between 0.2 and 0.5. Feng et al.[17] simulated the dust flow process of a filter element via computational fluid dynamics (CFD) by using a 2D model and found that the pressure drop of the filter element is proportional to the flow rate. In summary, studies on improving the dust removal efficiency of filters have been widely investigated. However, most of the related methods are based on indoor tests, and the reliability in natural gas station applications has yet to be reported.

In this study, an efficient method that combines online dust detection and numerical simulation were applied. A three-dimensional natural gas filter numerical model was first established based on the computational fluid dynamics theories. The characteristics of pressure drop and dust removal efficiency were investigated under different operating pressures, operational times, and flow rates. Both the simulation and experimental methods were proven to have good accuracy and reliability. The research results can provide a robust basis for improving the dust removal efficiency and working status of filter separators.

## 2. EXPERIMENTS

**2.1. Apparatus.** A filter separator was used to remove the dust particles in the gas flow, which is crucial to all of the gas transmission stations. The structure characteristics of the filter separator are shown in Figure 1. It mainly consists of a cylindrical separator with an inner diameter of 900 mm, an inlet with 350 mm inner diameter, an outlet, two differential pressure gauges, and two sewage pipes.

The internal structure and filtration mechanism are shown in Figure 2a. It can be found that 30 filter elements are arranged in a coalescence chamber. Gas containing dust particles flows into the coalescence chamber, where they are removed by the filter elements. Then, the dust particles flow out from the coalescence chamber into the gas collection chamber and are then transmitted to the downstream pipeline. Differential pressure gauges installed in the coalescence chamber and collection chamber, respectively, are used to detect the differential pressure created by the filter elements.

The basic size, material, and structure of a single internal filter element are presented in Figure 2b and Table 1. The

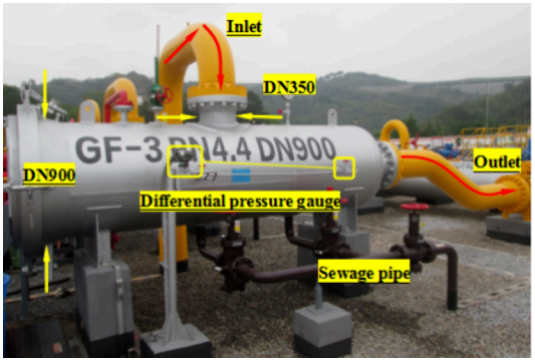


**Figure 1.** Typical filter separator used in a gas transmission plant.

length of the inner filter element is 1800 mm, and its inner and outer diameters are 96 and 114 mm, respectively. The materials are polyethylene fiber with a steel skeleton, and the operating temperature is between −5 and 115 °C. The filtration area of a single filter element is 2.98 $m^2$.

The initial pressure drop was tested with clean air passing through the filter cartridge, which is the differential pressure between the inside and outside of the filter. In the filter separator, the cartridges were arranged closely in a very limited space as if those cartridges formed a bigger new cartridge. Under this condition, the initial pressure drop may not be the same as that defined before. Further studies should be proposed to verify that its linear relationship of initial pressure drop still follows the Darcy's law.[18]

**2.2. Methods.** To investigate the dust removal efficiency $\eta_{eff}$, the dust concentrations of the inlet (upstream) and outlet (downstream) can be measured using a high-pressure particle size distribution detector and its efficiency can be expressed as below[18]

$$\eta_{eff} = 1 - \frac{C_{V,out}}{C_{V,in}} \quad (1)$$

where $C_{V,out}$ and $C_{V,in}$ are the outlet and inlet dust concentrations ($\mu m^3/m^3$), respectively.

The procedure for the detection process is shown in Figure 3. The process is composed of the sampling system (①), particle detection system (②), offline particle collection system (③), flow control system (④), and data acquisition system (⑤).[19]

In the sampling system, the nozzle is designed based on the standard ANSI/ASME PTC 38-1980 (determining the mass flow rate of particulate matter in a gas stream) and is inserted into the gas pipe with the inlet section perpendicular to the direction of gas flow. Then, the particle-sampling gas flows into a flow assignment room, where the gas temperature and pressure are monitored in real time by two high-precision sensors. Additional details of this sampling device can be found in the reference by Xiong et al.[20]

**2.3. Experimental Procedure.** Test numbers GF-1 to GF-5 were introduced to study the filter element's behavior under different operational conditions. The inlet pressures are 2.5, 3.5, 4.5, 2.5, and 2.5 MPa, respectively. The sampling analysis shows that the dust particles are irregular, with a particle size of 3−50 $\mu$m, and exhibits a normal distribution, as shown in Figure 4.

The average flow rate, the gas density, and the corresponding operating conditions are provided in Table 2.


https://doi.org/10.1021/acsomega.3c04202
ACS Omega 2023, 8, 36986−36998

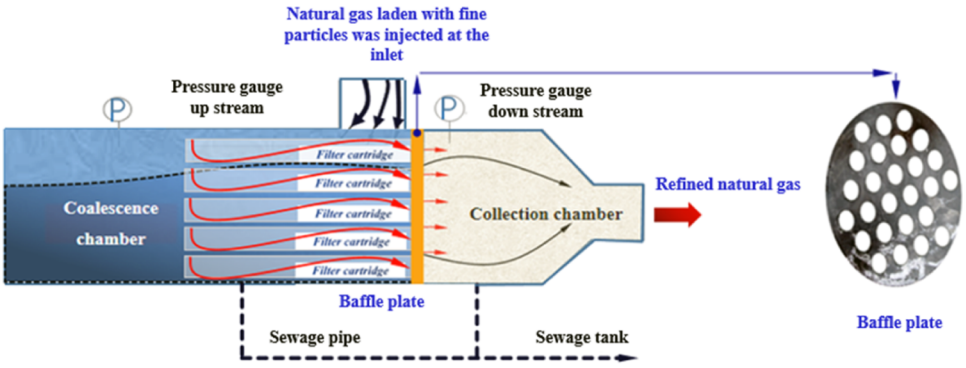


(**a**) Working principle of a filter separator.

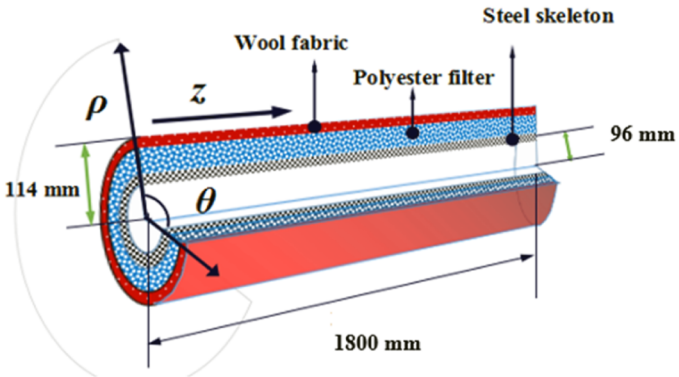


(**b**) Basic parameters of a single internal filter element.

**Figure 2.** (a) Working principle of a filter separator and its internal structure. (b) Basic parameters of a single internal filter element.

**Table 1. Structure Performance of Fibrous Medium**

| number of cartridges | filter fabric | thickness (mm) | color | longitude | initial pressure drop (kPa) | operational temperature (°C) | filtration area ($m^2$) |
|---|---|---|---|---|---|---|---|
| 30 | polyester fiber | 16.0 | white | 1800 | 13 | −5 to 115 | 2.98 |

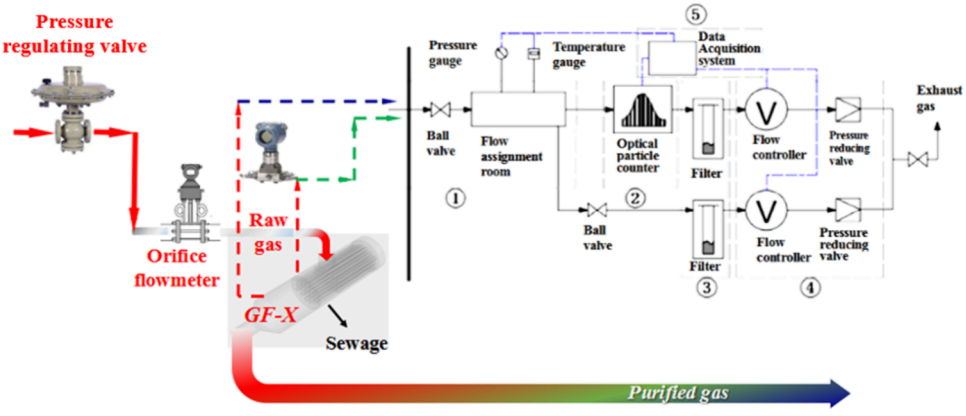


**Figure 3.** Particle detection device for high-pressure natural gas.

The dust removal efficiency of the filters was investigated by the particle size distribution detector in 1 month, 6 months, and 12 months after the filter element was installed and operated.

In addition to detecting the dust removal efficiency, the flow rate, operating pressure, and temperature of each filter were also recorded. The recording frequency is two times a week and the duration is 12 months, which aims to explore the effects of flow rates on the pressure drop.



https://doi.org/10.1021/acsomega.3c04202
ACS Omega 2023, 8, 36986−36998

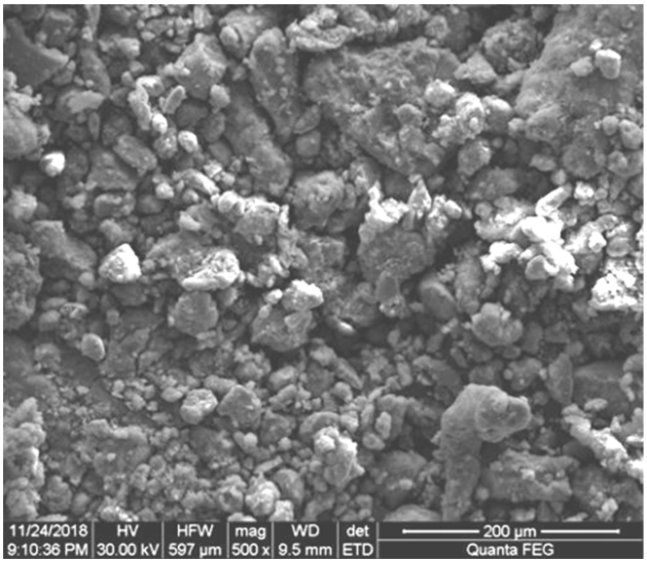


**Figure 4.** Microstructure of the dust particle.

## 3. NUMERICAL SIMULATION

**3.1. Mathematical Model Description.** The numerical simulation of the gas-particle flow was conducted via ANSYS fluent 15.0, and the Euler−Euler model was applied. Different phases were taken as continuous media, which interpenetrate with each other. The Euler equations were given as eq 2 and eq 3. The transient continuity equation and the momentum equation of the gas and solid phases were solved in accordance with the volume fraction.[21]

Continuity equation (with each phase solved separately):

$$\frac{\partial}{\partial t}(\alpha_k \rho_k) + \nabla\cdot(\alpha_k \rho_k \vec{u_k}) = 0 \tag{2}$$

Momentum equation (with each phase solved separately):

$$\frac{\partial}{\partial t}(\alpha_k \rho_k \vec{u_k}) + \nabla\cdot(\alpha_k \rho_k \vec{u_k}\vec{u_k}) = -\alpha_k \nabla p + \nabla\cdot\bar{\bar{\tau}}_k + \alpha_k \rho_k \vec{g} + \vec{F_D} + \vec{F_L} + \vec{F_{VM}} \tag{3}$$

where $\vec{u_k}$ is the velocity vector of each phase, $\bar{\tau}_k$ is the stress tensor of each phase, and $\rho_k$ is the density of each phase, which is written in the following constitutive equation:

$$\bar{\bar{\tau}}_k = -P_s\bar{\bar{I}} + \alpha_k\mu_k(\nabla\vec{u_k} + \nabla\vec{u_k}^T) + \alpha_k(\lambda_s - \frac{2}{3}\mu_k)\nabla\cdot(\vec{u_k}\bar{\bar{I}}) \tag{4}$$

$P_s$ is the pressure when the particle phase is continuous. It mostly occurs at the boundary between the fluid domain and the wall.

$$P_s = \alpha_s\rho_s\theta_s(\omega + 2(1 + e_s)\alpha_s g_o(\alpha_s)) \tag{5}$$

$\omega$ is the momentum and mass transfer of the particle flow.

$$\omega = \left(1 + \frac{d_s}{6\alpha_s D\sqrt{2}}\right) \tag{6}$$

$g_0(\alpha_s)$ is the radial distribution equation of particles. It is used to correct the probability of particle collision.

$$g_0(\alpha_s) = \frac{1}{1 - \alpha_s} + \frac{3\alpha_s}{2(1 - \alpha_s)^2} \tag{7}$$

$\mu_k$ is the shear viscosity caused by particle collision and translation.

$$\mu_k = \mu_{s,coll} + \mu_{s,kin} \tag{8}$$

The shear viscosity caused by particle collision is

$$\mu_{s,coll} = \frac{5d_s\rho_s(\theta_s\pi)^{1/2}}{96\alpha_s}([\frac{8\alpha_s}{5(2 - \eta)}][1 + \frac{8}{5}\eta(3\eta - 2)\alpha_s g_0(\alpha_s)] + \frac{768}{25\pi}\eta\alpha_s^2 g_0(\alpha_s)) \tag{9}$$

The shear viscosity caused by particle translation is

$$\mu_{s,kin} = \frac{5d_s\rho_s(\theta_s\pi)^{1/2}}{96\eta g_o(\alpha_s)}[1 + \frac{8}{5}g_o(\alpha_s)\alpha_s\eta] \tag{10}$$

$\lambda_s$ in eq 4 is the volume viscosity that characterizes the volume expansion of the solid phase

$$\lambda_s = \frac{4}{3}\alpha_s\rho_s d_s g_o(\alpha_s)(1 + e_s)(\frac{\theta_s}{\pi})^{1/2} \tag{11}$$

where $\alpha_s$ is the volume fraction of the particle phase, $e_s$ is the elastic coefficient, and $d_s$ is the particle size. The coefficient $\eta$ can be expressed as

$$\eta = (1 + \alpha_s)/2 \tag{12}$$

On the right side of eq 3, $\vec{F_D}$ is the drag force between the gas and solid phases

$$\vec{F_D} = \frac{3}{4}\alpha_k\rho_k\mu_k\frac{C_d Re_p}{d_p^2}(\vec{u_p} - \vec{u_k}) \tag{13}$$

$$Re_p = \frac{\rho d_p(u_p - u_k)}{\mu} \tag{14}$$

where $C_d$ is the drag coefficient of the single particle, $Re_p$ is the Reynolds number of a particle, $d_p$ is the particle diameter, $\alpha_k$ is the volume fraction of each phase, and $\vec{u_p}$ is the velocity of the

**Table 2. Online Detection Experimental Conditions**

| no. | inlet pressure (MPa) | flow rate ($10^4$Nm$^3$/d) | particle size ($\mu$m) | inlet velocity (m/s) | gas density (kg/m$^3$) | operating time (month) |
|---|---|---|---|---|---|---|
| GF-1 | 2.5 | 150−400 | 0−50 | 8.2−23.4 | 20.54 | 1, 6, 12 |
| GF-2 | 3.5 | | | 5.7−16.3 | 28.76 | |
| GF-3 | 4.5 | | | 4.4−12.4 | 36.98 | |
| GF-4 | 2.5 | 100−270 | | 7.8−20.9 | 20.54 | |
| GF-5 | 2.5 | 40−160 | | 3.1−12.4 | | |



https://doi.org/10.1021/acsomega.3c04202
ACS Omega 2023, 8, 36986−36998

solid phase. The drag coefficient model of Schiller and Naumann[22] is introduced into $\overrightarrow{F_D}$, as follows:

$$C_d = \max\left(\frac{24}{Re_p}\left(1 + 0.15Re_p^{0.687}\right), 0.44\right) \quad (15)$$

$\overrightarrow{F_L}$ is the lifting force applied by the gas phase to the solid phase.

$$\overrightarrow{F_L} = 1.615\alpha_k d_p \mu_k C_L Re_{si}^{0.5}(\overrightarrow{u_k} - \overrightarrow{u_p}) \times (\nabla \times \overrightarrow{u_k}) \quad (16)$$

$$C_L = \begin{cases} (1 - 0.3314\beta^{0.5})\exp(-0.1 \times Re_p) + 0.3314\beta^{0.5} & Re_p \le 40 \\ 0.0524(\beta Re_p)^{0.5} & Re_p > 40 \end{cases} \quad (17)$$

$$Re_{si} = \frac{\rho d_p^2(\nabla \times u_k)}{\mu_k} \quad (18)$$

$$\beta = \frac{Re_{si}}{0.5Re_p} \quad (19)$$

$$\overrightarrow{F_{vm}} = 0.5\rho_k\alpha_k\left(\frac{d\overrightarrow{u_p}}{dt} - \frac{d\overrightarrow{u_k}}{dt}\right) \quad (20)$$

To investigate the coalescence process in a numerical way, the source term $S_i$ was added to the right side of the momentum equation:[23]

$$S_i = -(B + A\cdot\vec{v_s}) \quad (21)$$

$$A = C_2\frac{1}{2}\rho\vec{v_s} \quad (22)$$

$$B = \frac{\mu}{a}\vec{v_s} \quad (23)$$

where $S_i$ is the source term in the direction of $i$ and $\vec{v_s}$ is the velocity vector of the particle. The first term $B$ on the right side of the equation is the Darcy flow term, and the second term on the right side of equation $A$ is the inertial resistance term. This source term is supposed to lead to a change in dust speed, pressure gradient, which, in turn will achieve a dust coalescence on the filter element. $a$ is the permeability, and $C_2$ is the coefficient of inertial resistance. The coefficients of inertial resistance and viscous resistance can be obtained through the relationship between pressure drop and velocity, as shown in eq 24

$$\Delta p = A\cdot\vec{v_s}^2 + B\cdot\vec{v_s} \quad (24)$$

Three filter separators GF-1, GF-2, and GF-3 were considered in the numerical simulation. The relationships between the initial pressure drop and the velocity were obtained by the curve fitting presented in Table 3. All of the correlation indexes $R^2$ are approximately 0.98. During the fitting process, the values of $A$ and $B$ should be greater than 0. Viscous resistance VR and inertial resistance IR can be expressed as eq 25 and eq 26

**Table 3. Coefficients Obtained for the Inertial and Viscous Resistance**

| filter separators | A | IR | B | VR | porosity |
|---|---|---|---|---|---|
| GF-1 | 0.062 | 0.0070 | 0.05812 | 7567 | 0.9 |
| GF-2 | 0.051 | 0.0074 | 0.04441 | 578 | |
| GF-3 | 0.018 | 0.0026 | 0.25 | 325 | |

$$VR = \frac{1}{a} = \frac{B}{\mu\Delta n} \quad (25)$$

$$IR = C_2 = \frac{2A}{\rho\Delta n} \quad (26)$$

The values of the parameters in the equations above are given in Table 4.

**Table 4. Basic Parameters and Data Sources for Equations 2−26**

| parameters | parameter significance | corresponding values |
|---|---|---|
| $a_k$ | volume fraction of gas and solid phases (%) | Gas phase: 99.99; solid phase: (2.7−8.0) × $10^{-10}$ |
| $\rho_k$ | density of gas and solid phases (%) | Gas phase: 20.54−36.98; solid phase: 3880 |
| $\mu_k$ | bulk viscosity (kg/(m·s)) | Gas phase: 1.19 × $10^{-5}$; particle phase: 1.19 × $10^{-8}$ |
| $a$ | permeability | 0.98 |
| $d_p$ | particle diameter ($\mu$m) | 0−50. The median particle size is 25. |
| $\overrightarrow{u_p}$ | velocity of the solid phase (m/s) | Determined by the initial conditions of mass flow. The value is provided in Table 2. |
| $\overrightarrow{u_k}$ | velocity of the gas phase (m/s) | |
| $D$ | pipe diameter (m) | See Figure 1 for the size of the geometric model |
| $\theta_s$ | viscosity coefficient of particles | Obtained by consulting the particle viscosity resistance coefficient and the Reynolds number curve[24,25] |
| $\triangle n$ | filter cloth thickness (mm) | See Table 1 |

**3.2. Model Solution.** A hybrid mesh was generated, as shown in Figure 5. The unstructured grid number of the filter chamber are approximately 410,000, and the structured grid number of the filter cartridges are approximately 130,000 grids.

Turbulent kinetic energy and turbulent dissipation rate were set as 5 and 10%, respectively. The outlet pressure was set the same as the inlet pressure because the maximum pressure drop of the filter separator is only tens of kilopascals. The particle size distribution of the dust particles was compiled into the particle size of the second phase through macro DEFINE_PROPERTY in the user defined function. The SIMPLE algorithm was used to obtain the velocity and pressure drops of each phase. The momentum equations of each phase were discretized by the first-order upwind method, and the second-order upwind algorithm was used to obtain the turbulent kinetic energy and turbulent diffusion rate. The time step was set as $10^{-4}$ s, and 2 × $10^5$ steps were incorporated until the simulation was converged. Finally, the filtration process in 12 months can be achieved by increasing the time step. The convergence criterion was determined as follows:

$$\Phi_{inlet} - \Phi_{outlet} = \frac{M}{t} \quad (27)$$



https://doi.org/10.1021/acsomega.3c04202
ACS Omega 2023, 8, 36986−36998

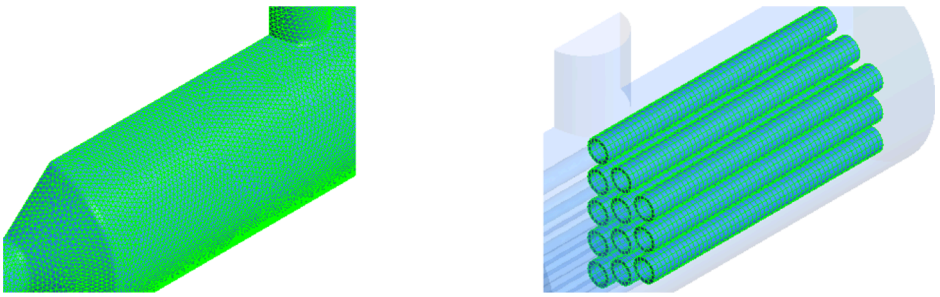

(a) (b)

**Figure 5.** Hybrid mesh with partial geometry: (a) partial mesh of the filter separator; (b) partial mesh of the internal filter elements.

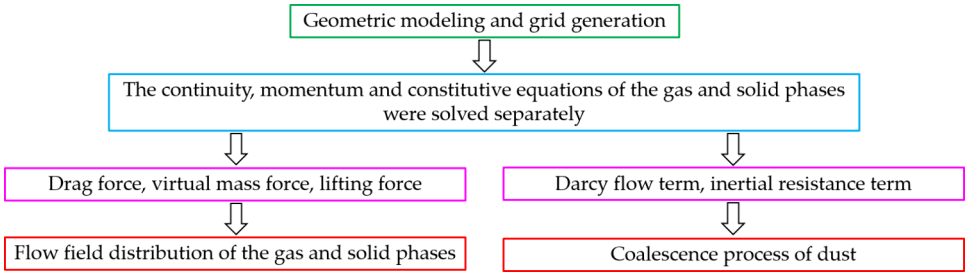


**Figure 6.** Flowchart for the model solution.

where Φ is the dust mass flow, kg/s; $M$ is the collected dust mass, kg; and $t$ is the operating time, s.

It is also worth explaining the operational time captured in the simulation. The transient method was used for the calculation, and the time setting was consistent with the actual operating time of the on-site filter. After the operation converged, the pressure drop between the inlet and outlet of the filter was established and the particles entering and exiting the filter reached dynamic equilibrium. Then, to synchronize with the real time, the step size was enlarged, and the model established can be calculated.

The solution process of abovementioned models is illustrated in Figure 6. First, the physical model and the corresponding grids were established. Then, the continuity, momentum, and constitutive equations of the gas and solid phases were solved simultaneously. The Darcy flow terms and inertial resistance terms were then identified by introducing the values in Table 3 and Table 4. The gas flow field, the solid phase distribution, and the filtration process of the filter element were obtained.

The calculation accuracy usually increases with increasing the grids, but the balance between the accuracy and calculation time needs to be taken into account.[26] A mesh independence study was conducted to ensure that the mesh resolution did not significantly affect the results of the numerical simulation. To this aim, the GF-2 model was meshed using different numbers of grids (between 250,000 and 750,000). The distortion of all the grids is between 0 and 0.4, indicating that the grids are with good quality.

Figure 7 shows the coalescence process of the particle flow when GF-2 was operated for 0.5 s under different numbers of grids. A certain difference can be noted in the coalescence process when the number of grids are between 250,000 and 430,000. By contrast, the coalescence process remains basically the same when the grids increase from 540,000 to 750,000.

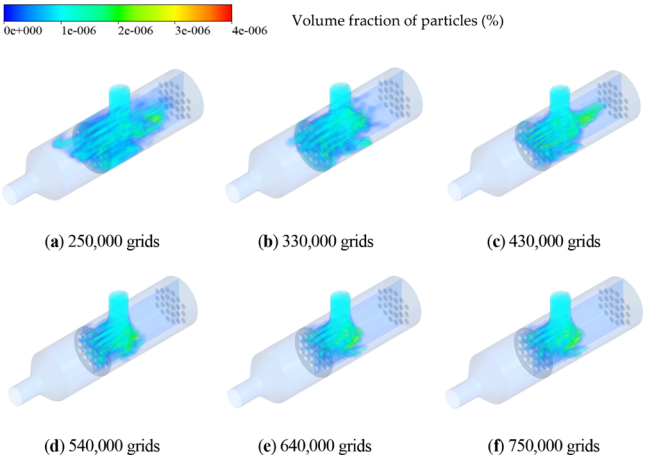


**Figure 7.** (a−f) Coalescence process of particle phase flow when filter separator GF-2 was operated for 0.5 s under different grid numbers.

Therefore, the mesh of 540,000 grids can lead to relatively high simulation accuracy in a reasonable simulation time.

Figure 8 shows the changes in the dust volume concentration at the outlet of the filter when the filter separator GF-2 was operated for 11 s under different grid numbers. It can be also indicated that the outlet dust volume concentration tends to be stable when the number of grids is greater than 540,000; hence, the reasonable grid number can be determined as 540,000.

## 4. RESULTS AND DISCUSSION

**4.1. Effect of Operational Pressure on the Gauge Pressure Drop.** The gauge pressure drops and flow rates of GF-1, GF-2, and GF-3 were recorded during the first month in use. The effect of the flow rate on the pressure drop is presented in Figure 9. It can be found that the pressure drops of the three filters generally increase with increasing flow rates.



https://doi.org/10.1021/acsomega.3c04202
ACS Omega 2023, 8, 36986−36998

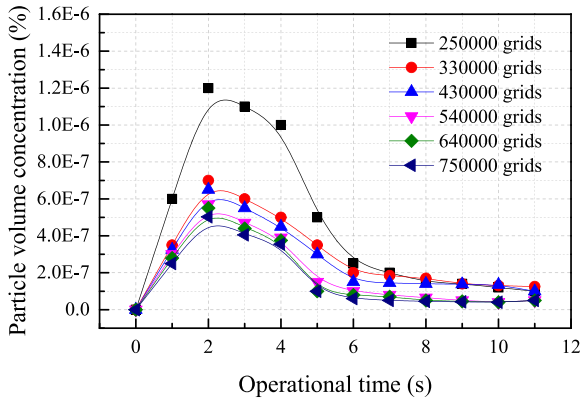


**Figure 8.** Change in dust volume concentration at the outlet of the filter when filter separator GF-2 was operated for 11 s under different grid numbers.

When the corresponding plots are presented in terms of dimensionless Euler number ($Eu = \Delta P/(\rho V^2)$) vs Reynolds number ($Re = \rho VL/(\mu)$), a trend similar to that in terms of pressure drop vs flow rate in Figure 9 can be also obtained. Under the same operational flow rates of 150−400 × $10^4$ $Nm^3/d$, the pressure drop measured in GF-3 is the lowest but that in GF-1 is the highest. The reason is that the lower operating pressure generally leads to a faster particle flow velocity and a higher local resistance under the same flow rate.

Figure 9 shows the comparison of the experimental pressure drop with the simulated data at different operational flow rates. The simulated values are generally lower than those fitted by the experimental data. It can be attributed to the fact that the particles intermittently enter the filter fiber and then flow out through the weak pores of the filter material in actual operation of the filter.[13] This will cause disturbance of the pressure drop, resulting in an increase in the relative error of the pressure monitoring device and a slow decrease in the pressure drop. However, the process in which particles "find" weak fiber pores in the actual flow is difficult to describe through the CFD method. In accordance with the settings of the source term in eq 21, the resistance characteristics of the filter element can only be described linearly.[10] It can be noted from the simulation results that the relative errors of the pressure drop simulated increase with increasing operating flow rate. Nevertheless, the maximum error can still be controlled within ±20%, which indicates that the initial pressure drops in the filter separator within 1 month can be accurately predicted using the simulation method.

**4.2. Effect of Operational Time on the Gauge Pressure Drop.** Figure 10a−c shows the gauge pressure drops of the GF-1, GF-2 and GF-3 filter separators under operating times of 1, 6, and 12 months, respectively. For both the pressure drops obtained from online testing and numerical simulation, it can be found that the gauge pressure drops generally gradually increase with the flow rate for all the three

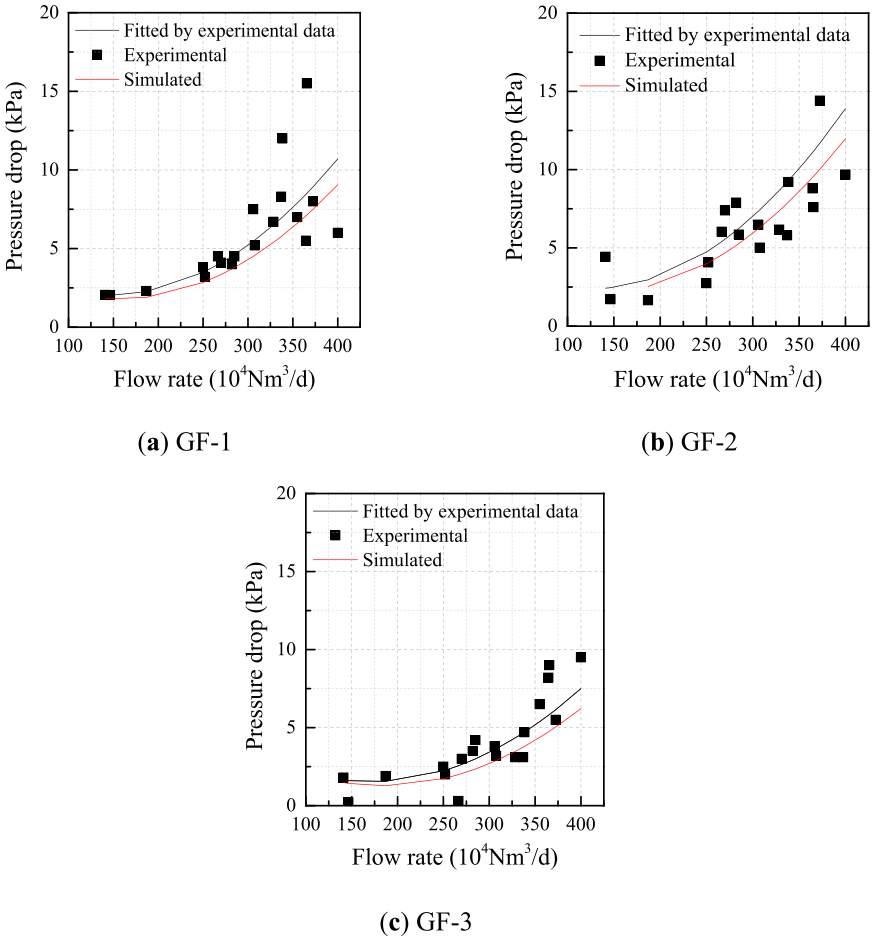


**Figure 9.** (a−c) Comparison of the simulated and experimental pressure drops at different flow rates for the filter separators during the first month in use.



https://doi.org/10.1021/acsomega.3c04202
ACS Omega 2023, 8, 36986−36998

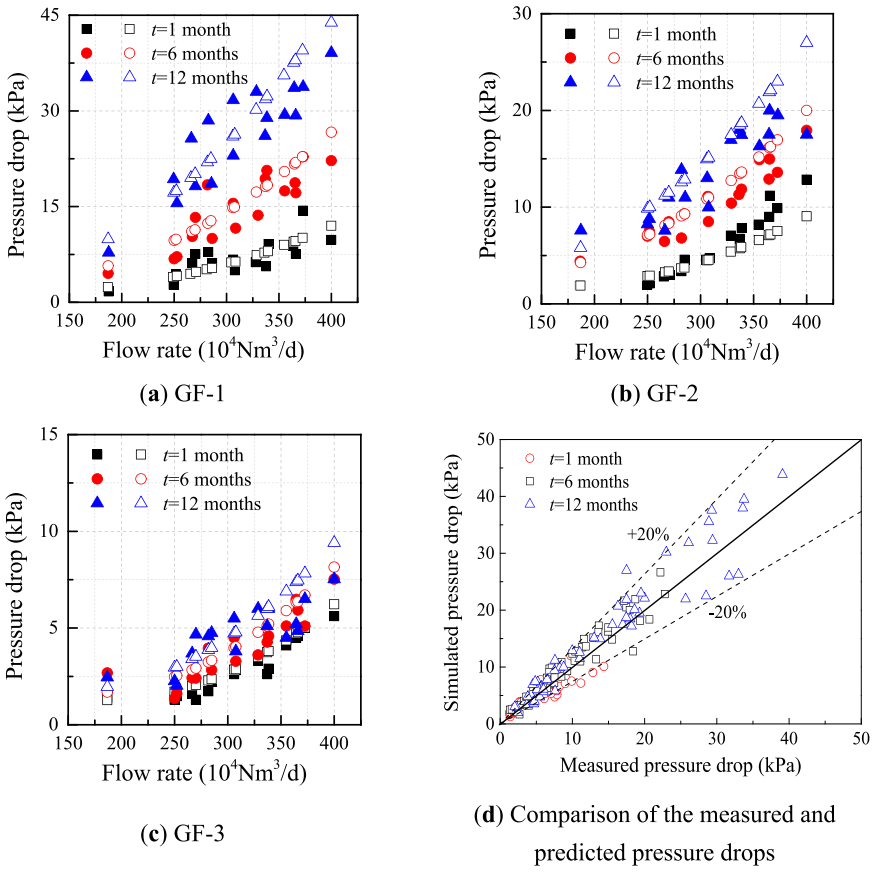


**Figure 10.** (a−d) Effect of operating time on the pressure drop (the solid symbols represent the data obtained through online testing, and the hollow symbols represent the data obtained by numerical simulation).

filter separators studied. A higher pressure drop can be obtained for a longer operating time at fixed operating pressures and the coalescence amount of dust also increase as the operating time increases. The detection pressure drop point will continuously deviate from the fitted optimal quadratic curve, and the correlation coefficient $R^2$ becomes smaller. In addition, the increase rates of pressure drops for GF-2 and GF-3 under higher operating pressures are lower than those for GF-1 under lower operating pressures. It can be explained that the lower the gas velocity, the smaller the resistance under the same friction coefficient.

What is more, it can be also found that the higher the operating pressure, the lower the gauge pressure drop in both simulation and experimental results. Compared with the experimental pressure drops shown in Figure 10d, the relative errors between the simulated and experimental values are basically within ±20%. This indicates that the simulation method could provide a relatively reliable prediction of the gauge pressure drop of filter separator over time.

**4.3. Effect of Flow Rate on the Gauge Pressure Drop.** The effect of flow rate on the gauge pressure drop was experimentally investigated under the same dust concentration, physical properties of the filter element, operating pressure, and temperature. As shown in Figure 11, three filter separators GF-1 with an operating flow rates from 150 to 400 × $10^4$ $Nm^3/d$, GF-4 with an operating flow rates from 100 to 270 × $10^4$ $Nm^3/d$, and GF-5 with an operating flow rates from 40 to 160 × $10^4$ $Nm^3/d$ were taken into consideration, and all the gauge pressure drops tend to increase with an increase in gas flow rate after 12 months of operation. The detected gauge

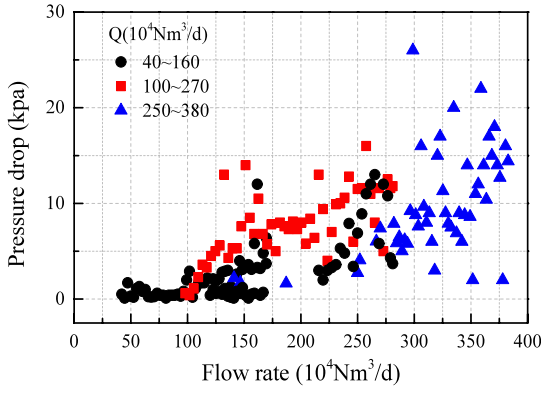


**Figure 11.** Effect of flow rate on the gauge pressure drop for 12 months of operation.

pressure drops become more scattered with increasing gas flow rates and velocities.

**4.4. Effect of Operating Time on the Dust Removal Efficiency.** The effects of operating time on the dust removal efficiency of filters GF-1, GF-2, and GF-3 are presented in Figure 12a−c. From both the results obtained by online testing and simulation, the efficiencies are basically the same at the initial moment of 1 month. As the operating time increases, the dust removal efficiency gradually reduces. In particular, the efficiency of GF-1 declines at the fastest rate when the operating pressure is fixed at 2.5 MPa, whereas the efficiency of GF-3 reduces at the slowest rate when the operating pressure increases to 4.5 MPa. This can be attributed to the fact that the


https://doi.org/10.1021/acsomega.3c04202
ACS Omega 2023, 8, 36986−36998

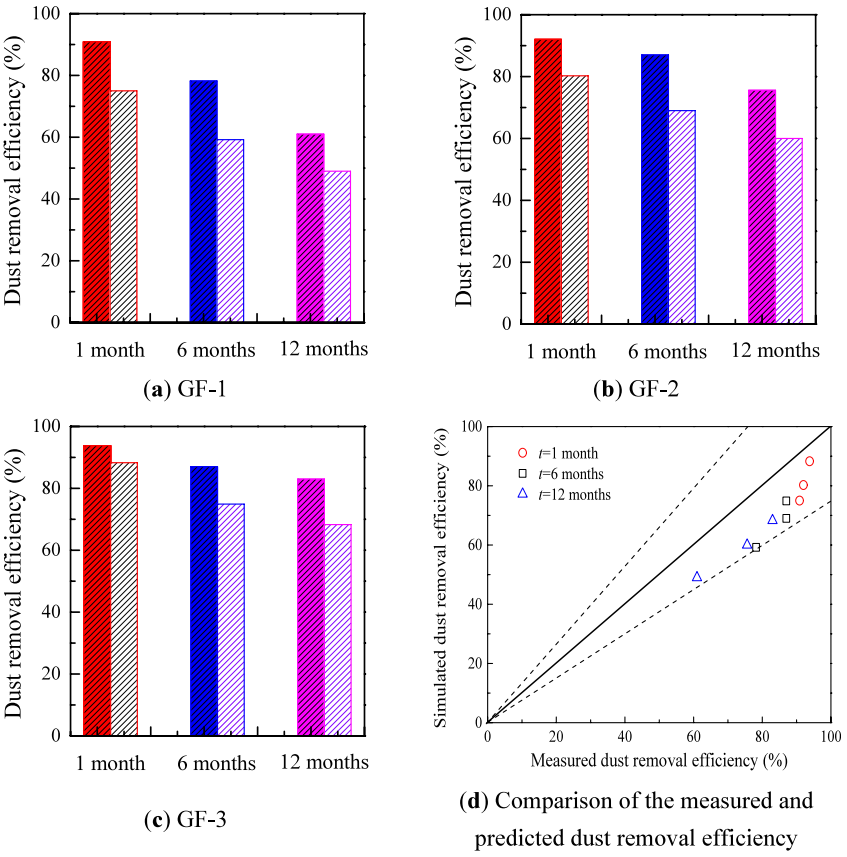


**Figure 12.** (a–d) Effect of operating time on the dust removal efficiency of each filter separator (the solid columns represent the data obtained through online testing, and the hollow columns represent the data obtained by numerical simulation).

GF-1 filter has a faster velocity, and thus more agglomerated particles will be rushed out from the filter separator in operation, which leads to an increasing dust concentration at the downstream. As shown in Figure 12d, all the relative errors between the simulated efficiencies and measured values are within ±20%, which indicates that the simulation method is an effective way to determine the dust removal efficiency of filter separators.

Mouret et al.[27] found that when the pore size of the filter element increased from 400 $\mu$m to 2 mm, the corresponding flow rate increased by 7 times, while the dust removal efficiency of 5 nm particles decreased to one-ninth. What is more, larger pore sizes are more likely to cause higher particle passing rates, making the filter material easier to be destroyed. Xu et al.[28] explored that the pressure drop of the filter element exhibited a linear relationship with the inlet velocity and the slope $k$ of which was approximately 0.7. When the adsorption capacity of the filter element is saturated, the loss of the filter material per unit time is increased with increasing flow rate. Figure 13 shows the surface morphologies of the GF-1 and GF-3 filter elements after 12 months of usage. The surface of the filter element was crushed and deformed under low pressure and high gas velocity, indicating that the filter material is more likely to be damaged under low pressure.

### 4.5. Effect of Flow Rate on Dust Removal Efficiency.

The effect of flow rate on the dust removal efficiency and particle proportion at different operating times is shown in Figure 14. Here, $dN/N$ is defined as the ratio of the number of particles with a certain particle size to the total number of particles detected. From Figure 14a, it can be found that when


**Figure 13.** Surface morphologies of the filter elements after 12 months of operation under different pressures. (a) Original filter element; (b) surface of the filter element operating at 4.5 MPa (GF-3); (c) surface of the filter element operating at 2.5 MPa (GF-1).

the GF-1 separator with a flow rate of 150–400 × $10^4$ $Nm^3/d$ was operated for 1 month, particles with sizes greater than 1.7 $\mu$m at the outlet only account for a relatively small proportion. When the operating time was extended to 6 months, the average proportion of particles with sizes greater than 1.7 $\mu$m gradually increased to about 10%. After 12 months of operation, the proportion of particles at the outlet reached 30%. Correspondingly, the dust removal efficiency slightly increased from 94 to 96% in the first 6 months but then rapidly declined to 30% at after one year of operation. This indicates


https://doi.org/10.1021/acsomega.3c04202
ACS Omega 2023, 8, 36986–36998

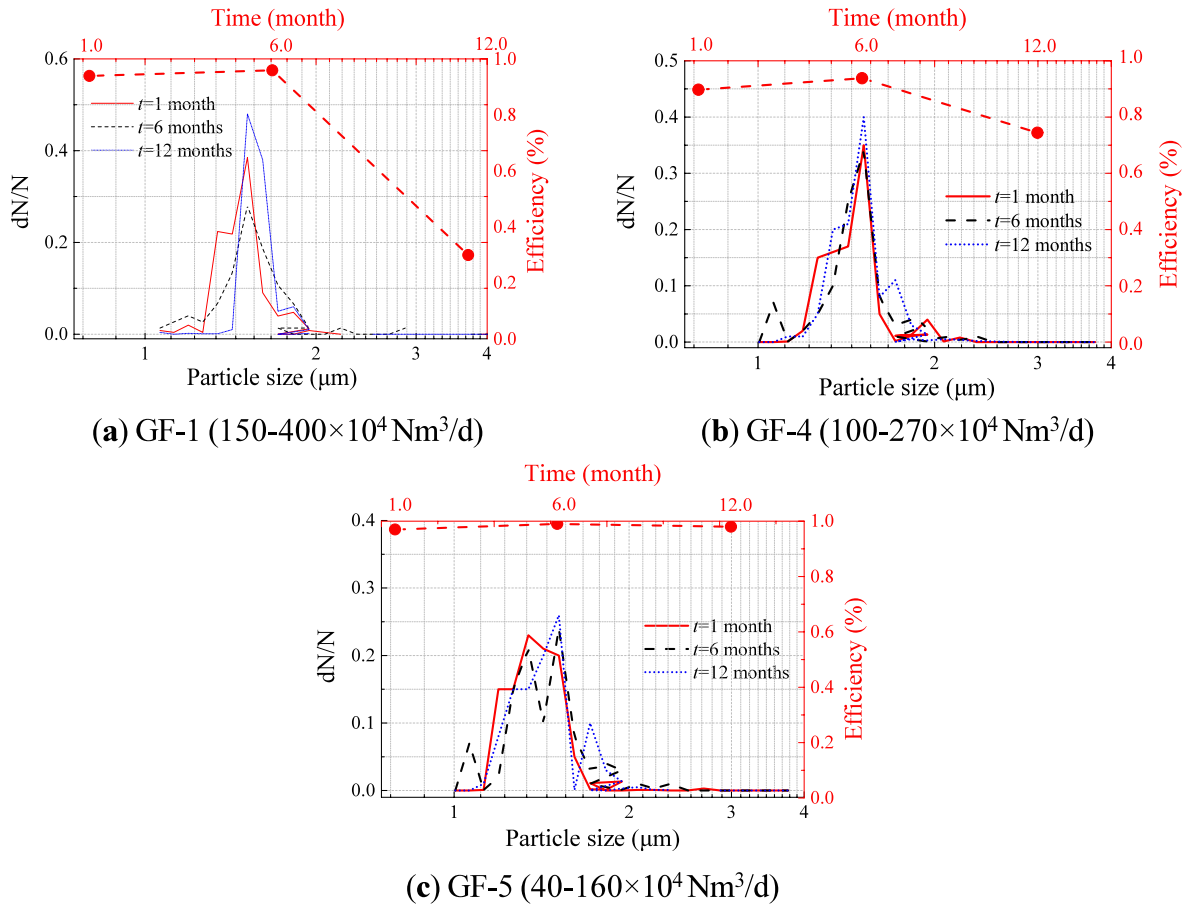


**Figure 14.** Effect of flow rate on the dust removal efficiencies and particle proportion of (a) GF-1, (b) GF-4, and (c) GF-5 separators after 12 months of operation.

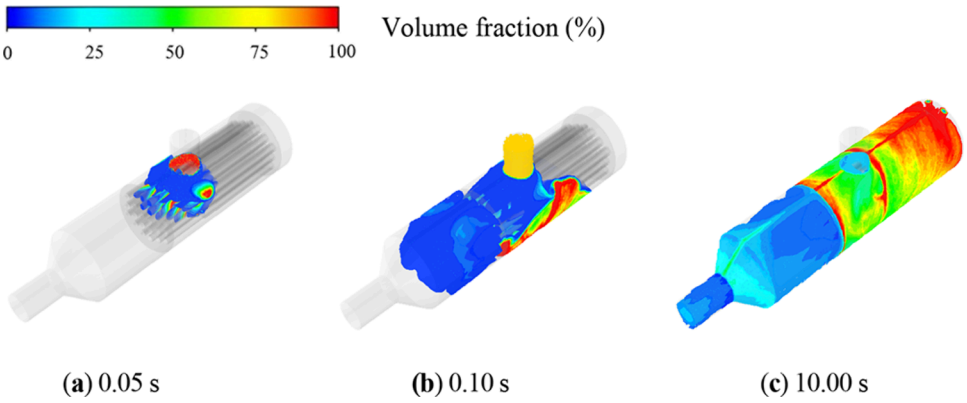


**Figure 15.** (a–c) Coalescence process of the dusts.

that the dust removal efficiency generally reduces with the increase in the proportion of large particles.

As shown in Figure 14b, when the flow rate of the GF-4 separator was controlled in the range 100–270 × $10^4$ $Nm^3/d$, the efficiency initially increased from 90 to 94% and then decreased to about 80% during 12 months of testing. In the entire process, the particle proportions at the three time points were relatively close, with an average ratio of approximately 15% maintained. It can also be seen from Figure 14c that the proportion of large particles at the outlet is low and the filter has great performance. This is because the interior of the filter element has not yet reached saturation, and there are still lot of unused pores. The general dust removal efficiency in the test period is maintained above 95%. Considering the flow rate, dust removal efficiency, cost of filter separator, and differential pressure comprehensively, a reasonable gas flow rate of 100–270 × $10^4$ $Nm^3/d$ is the recommended in the gas transmission.

**4.6. Flow Field Characteristics of Dust Flow.** Figure 15 shows the coalescence process of the dust flow of the GF-1 filter during the first 10 s. At the initial moment, the upstream dust volume fraction is 100% at 0.05 s, the downstream dust volume fraction maintained about 30% at 10.0 s, and the dust removal efficiency can reach approximately 70%. We can see that when the dusts just entered the filter separator, they



https://doi.org/10.1021/acsomega.3c04202
ACS Omega 2023, 8, 36986–36998

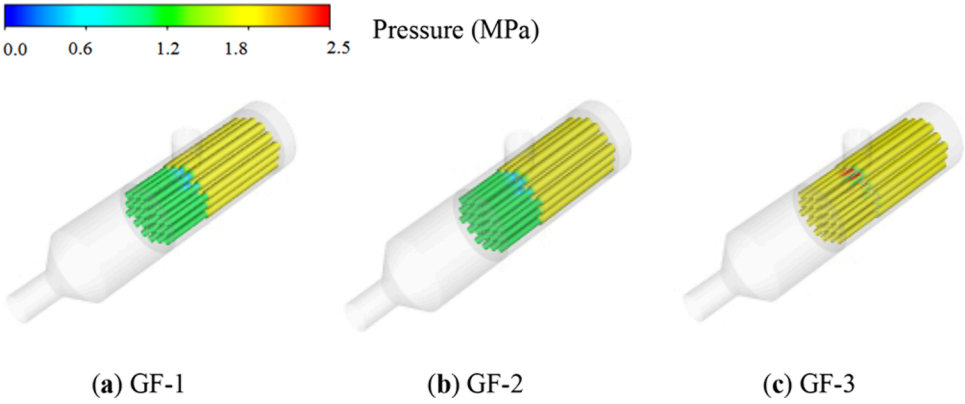


**Figure 16.** (a−c) Pressure distribution of dust on the surface of the filter element.

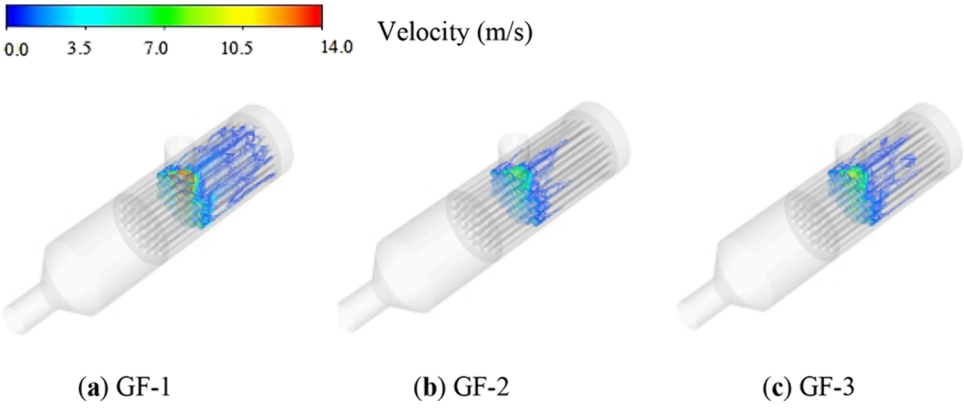


**Figure 17.** (a−c) Velocity distribution of dust on the surface of the filter element.

coalesced on the filter element closest to the inlet at 0.1 s and the dynamic balance of dust flow was observed after 10 s of operation. Subsequently, the dusts underwent complex flow under the action of turbulence before coalescing through the filter element and eventually entered the collection chamber. Therefore, the concentration of dust at the far end of the coalescence chamber is higher than that at the inlet and outlet of the coalescence chamber.

In Figure 16, the pressure in the GF-3 separator is mostly concentrated on the inlet side of the filter. In contrast with the GF-1 and GF-2 separators, the pressure is not rapidly released and a high flow rate zone will form. Moreover, it can be found from Figure 17 that as the operating pressure increases, the velocity on the surface of the filter element decreases from 14 to about 8 m/s. This also indicates that the rapid decrease in the dust removal efficiency of the GF-1 separator is related to the increase in flow velocity and the rapid passage of dust particles through the filter element. The areas with high surface flow velocity of the filter element are located in the tightly connected area between the filter aggregation chamber and the collection chamber, which is consistent with the damaged position of the filter element shown in Figure 13c.

## 5. CONCLUSIONS

Investigations on the dust removal efficiency of a natural gas filter via a pressure drop under different operational conditions were carried out experimentally and numerically, which could provide guidelines for the on-site operation and replacement of a filter in the filter separator. Based on the findings presented in this study, the following can be concluded:

(1) Under the same standard flow rate, the lower the operating pressure, the faster the gas velocity, the greater the local resistance of the filter separator, and the higher the pressure drop. This process can be effectively predicted by the computational fluid dynamics simulation method.

(2) As the operating time increases, the pressure drop of the filter separator will gradually deviate from the fitted optimal quadratic curve, and its dust removal efficiency will continue to decrease. A faster decrease in the dust removal efficiency occurs at lower operating pressures.

(3) Under the same operating pressure, the larger the gas flow rate, the more dispersed the pressured-drop points upstream and downstream of the filter separator, which continuously deviates from the fitted optimal quadratic curve. Moreover, the faster the dust removal efficiency decreases, the more large particles appear downstream.

(4) The dust removal efficiency of the filter separator obtained through the CFD simulation and experimental detection can effectively reflect its actual performance, and the relative errors of the experimental and simulated results are basically within ±20%. The actual dust removal amount on site can further confirm the accuracy and reliability of the two methods.

(5) Based on comprehensive consideration of the factors including gas flow rate, differential pressure, dust removal efficiency, etc., an economic and reasonable gas flow rate of 100−270 × $10^4$ $Nm^3/d$ is the recommended in the actual gas transmission.



https://doi.org/10.1021/acsomega.3c04202
ACS Omega 2023, 8, 36986−36998

## AUTHOR INFORMATION


### Corresponding Author

**Sijia Zheng** − *Gathering and Transmission Technology Research Institute of PetroChina Southwest Oil and Gasfield Company, Chengdu, Sichuan 610041, China;* orcid.org/0009-0003-1550-6514; Email: francis.22@163.com

### Authors

**Zhixiang Dai** − *Gathering and Transmission Technology Research Institute of PetroChina Southwest Oil and Gasfield Company, Chengdu, Sichuan 610041, China*

**Feng Wang** − *Gathering and Transmission Technology Research Institute of PetroChina Southwest Oil and Gasfield Company, Chengdu, Sichuan 610041, China*

**Qin Bie** − *Gathering and Transmission Technology Research Institute of PetroChina Southwest Oil and Gasfield Company, Chengdu, Sichuan 610041, China*

**Xinyi Wang** − *Gathering and Transmission Technology Research Institute of PetroChina Southwest Oil and Gasfield Company, Chengdu, Sichuan 610041, China*

**Xubing Liu** − *Gas Transportation Management Division of PetroChina Southwest Oil and Gasfield Company, Chengdu, Sichuan 610213, China*

**Lin Zhong** − *School of Mechanical Engineering, Southwest Petroleum University, Chengdu, Sichuan 610500, China*

Complete contact information is available at: https://pubs.acs.org/10.1021/acsomega.3c04202


### Author Contributions

All authors made substantial contributions to the manuscript. The manuscript to be submitted was approved by all the authors. The authors have done the following work: methodology, investigation, data curation, original draft preparation, S.Z.; investigation, methodology, Z.D.; investigation, validation, F.W.; data curation, review and editing, Q.B.; formal analysis, validation, X.W. formal analysis, review and editing, X.L.; data curation, review and editing, L.Z.

### Notes

The authors declare no competing financial interest.

## ACKNOWLEDGMENTS

This work was supported by the Major Science and Technology Project of the PetroChina Company Limited (2016E-0610).

## REFERENCES


(1) Zhang, X.; Cheng, S.; Huang, X.; Logan, B. E. The use of nylon and glass fiber filter separators with different pore sizes in air-cathode single-chamber microbial fuel cells. *Energy Environ. Sci.* **2010**, *3* (5), 659−664.

(2) Huang, F.; Xu, Y.; Peng, B.; Su, Y.; Jiang, F.; Hsieh, Y. L.; Wei, Q. Coaxial electrospun cellulose-core fluoropolymer-shell fibrous membrane from recycled cigarette filter as separator for high performance lithium-ion battery. *ACS Sustainable Chem. Eng.* **2015**, *3* (5), 932−940.

(3) Sandulyak, A. A.; Sandulyak, A. V.; Ershov, D. V. Separator filter for iron impurities in ceramic suspensions. Magnetic field in matrix pores. *Glass Ceram.* **2013**, *70* (5−6), 223−224.

(4) Lyu, L.; Zhang, J.; Xu, C. Modeling study on oil particle filtration performance of a composite coalescing filter. *Front. Energy Res.* **2022**, *10*, No. 854913.

(5) Feng, Z.; Zheng, W.; Chen, Q. Assessment of various CFD models for predicting airflow and pressure drop through pleated filter system. *Build. Environ.* **2014**, *75* (4), 132−141.

(6) Boulaud, D. Use of granular beds in the inertial impaction regime for aerosol size distribution measurement. *J. Aerosol Sci.* **1991**, *22*, 273−287.

(7) Thomas, D.; Penicot, P.; Contal, P.; Leclerc, D.; Vendel, J. Clogging of fibrous filters by solid aerosol particles experimental and modelling study. *Chem. Eng. Sci.* **2001**, *56* (11), 3549−3561.

(8) Song, C. B.; Park, H. S.; Lee, K. W. Experimental study of filter clogging with monodisperse PSL particles. *Powder Technol.* **2006**, *163* (3), 152−159.

(9) Ali, S. B.; Ghasemi, H.; Ahmadi, R.; Ghaffari, A. Recent progresses in dry gas polymeric filters. *J. Energy Chem.* **2021**, *62*, 103−119.

(10) Azam, M. S.; Niu, F.; Wang, D.; Zhuo, W. Experimental and CFD analysis of the effects of debris deposition across the fuel assemblies. *Nucl. Eng. Des.* **2018**, *332*, 238−251.

(11) Liu, Z.; Ji, Z.; Zhang, J.; Li, L. Influence of processing parameters on gas-liquid filtration performance of fibrous filter cartridge. *Procedia Eng.* **2015**, *102*, 911−920.

(12) Lim, T. H.; Yeo, S. Y.; Lee, S. H. Multidirectional evaluations of a carbon air filter to verify their lifespan and various performances. *J. Aerosol Sci.* **2018**, *126*, 205−216.

(13) Riefler, N.; Ulrich, M.; Morshäuser, M.; Fritsching, U. Particle penetration in fiber filters. *Particuology* **2018**, *40*, 70−79.

(14) Thomas, D.; Pacault, S.; Charvet, A.; Bardin-Monnier, N.; Appert-Collin, J. C. Composite fibrous filters for nano-aerosol filtration: Pressure drop and efficiency model. *Sep. Purif. Technol.* **2019**, *215*, 557−564.

(15) Thomas, D.; Penicot, P.; Contal, P.; Leclerc, D.; Vendel, J. Clogging of fibrous filters by solid aerosol particles experimental and modelling study. *Chem. Eng. Sci.* **2001**, *56* (11), 3549−3561.

(16) Bourrous, S.; Bouilloux, L.; Ouf, F. X.; Lemaitre, P.; Nerisson, P.; Thomas, D.; Appert-Collin, J. C. Measurement and modeling of pressure drop of HEPA filters clogged with ultrafine particles. *Powder Technol.* **2016**, *289*, 109−117.

(17) Feng, Z.; Long, Z.; Chen, Q. Assessment of various CFD models for predicting airflow and pressure drop through pleated filter system. *Build. Environ.* **2014**, *75* (4), 132−141.

(18) Davies, C. N. Diffusion and sedimentation of aerosol particles from poiseuille flow in pipes. *J. Aerosol Sci.* **1973**, *4* (4), 317−328.

(19) Lu, L.; Wu, X.; Ji, Z.; Xiong, Z.; Wang, M.; Song, X. Approach for correcting particle size distribution measured by optical particle counter in high-pressure gas pipes. *Appl. Opt.* **2018**, *57* (13), 3497−3506.

(20) Xiong, Z.; Ji, Z.; Wu, X.; Chen, Y.; Chen, H. Experimental and numerical simulation investigations on particle sampling for high-pressure natural gas. *Fuel* **2008**, *87*, 3096−3104.

(21) Adamczyk, W. P.; Klimanek, A.; Białecki, R. A.; Węcel, G.; Kozołub, P.; Czakiert, T. Comparison of the standard Euler-Euler and hybrid Euler-Lagrange approaches for modeling particle transport in a pilot-scale circulating fluidized bed. *Particuology* **2014**, *15* (4), 129−137.

(22) Chen, B.; Wang, B.; Mao, F.; Ke, B.; Wen, J.; Tian, R.; Lu, C. Review on separation mechanism of corrugated plate separator. *Ann. Nucl. Energy* **2020**, *144*, No. 107548.

(23) Havasi-Tóth, B. Particle coalescing with angular momentum conservation in SPH simulations. *Comput. Fluids* **2020**, *197*, No. 104384.

(24) Zhang, P.; Qiu, L.; Chen, Y.; Zhao, Y.; Kong, L.; Scheuermann, A.; Li, L.; Galindo-Torres, S. A. Coupled metaball discrete element lattice Boltzmann method for fluid-particle systems with non-spherical particle shapes: A sharp interface coupling scheme. *J. Comput. Phys.* **2023**, *479*, No. 112005.

(25) Gao, Z.; Duan, C.; Zhao, Y.; Mao, P. Apparent viscosity of mixed particle system in pulsed gas−solid separation fluidized bed. *Particuology* **2022**, *71*, 41−46.

(26) Hong, K.; Gao, Y.; Ullah, A.; Xu, F.; Xiong, Q.; Lorenzini, G. Multi-scale CFD modeling of gas-solid bubbling fluidization accounting for sub-grid information. *Adv. Powder Technol.* **2018**, *29* (3), 488−498.




https://doi.org/10.1021/acsomega.3c04202
*ACS Omega* 2023, 8, 36986−36998

(27) Mouret, G.; Thomas, D.; Chazelet, S.; Appert-Collin, J. C.; Bemer, D. Penetration of nanoparticles through fibrous filters perforated with defined pinholes. *J. Aerosol Sci.* **2009**, *40* (9), 762−775.
(28) Xu, C.; Xie, W.; Yu, Y.; Zhang, J.; Yang, J. Photocatalytic and filtration performance study of $TiO_2$/CNTs-filter for oil particle. *Process Saf. Environ. Prot.* **2019**, *123*, 72−78.



https://doi.org/10.1021/acsomega.3c04202
*ACS Omega* 2023, 8, 36986−36998